

Optimally graded porous material for broadband perfect absorption of sound

Cite as: J. Appl. Phys. **126**, 175101 (2019); <https://doi.org/10.1063/1.5119715>

Submitted: 11 July 2019 . Accepted: 13 October 2019 . Published Online: 05 November 2019

Jean Boulvert, Théo Cavaliere, Josué Costa-Baptista, Logan Schwan , Vicente Romero-García ,
Gwénaél Gabard , Edith Roland Fotsing , Annie Ross, Jacky Mardjono, and Jean-Philippe Groby 

COLLECTIONS

 This paper was selected as Featured



View Online



Export Citation



CrossMark

ARTICLES YOU MAY BE INTERESTED IN

[Optimally graded porous material for better sound absorption](#)

Scilight **2019**, 451103 (2019); <https://doi.org/10.1063/10.0000219>

[Acoustic metasurface-based perfect absorber with deep subwavelength thickness](#)

Applied Physics Letters **108**, 063502 (2016); <https://doi.org/10.1063/1.4941338>

[Grain growth stagnation and texture development in an irradiated thermally stabilized nanocrystalline alloy](#)

Journal of Applied Physics **126**, 175901 (2019); <https://doi.org/10.1063/1.5118943>

Lock-in Amplifiers

... and more, from DC to 600 MHz



Optimally graded porous material for broadband perfect absorption of sound



Cite as: J. Appl. Phys. 126, 175101 (2019); doi: 10.1063/1.5119715

Submitted: 11 July 2019 · Accepted: 13 October 2019 ·

Published Online: 5 November 2019



Jean Boulvert,^{1,2,3,a)} Théo Cavalieri,^{2,3} Josué Costa-Baptista,¹ Logan Schwan,²  Vicente Romero-García,² 
Gwénaél Gabard,²  Edith Roland Fotsing,¹  Annie Ross,^{1,b)} Jacky Mardjono,^{3,c)} and Jean-Philippe Groby^{2,d)} 

AFFILIATIONS

¹Laboratoire d'Analyse Vibratoire et Acoustique, LAVA, Mechanical Engineering, Polytechnique Montréal, Montréal, Québec H3T 1J4, Canada

²Laboratoire d'Acoustique de l'Université du Mans, LAUM—UMR CNRS 6613, Le Mans Université, Avenue Olivier Messiaen, 72085 Le Mans Cedex 9, France

³Safran Aircraft Engines, Villaroche, Rond Point René Ravaut—Réau, 77550 Moisy-Cramayel Cedex, France

^{a)}jean.boulvert@univ-lemans.fr

^{b)}annie.ross@polymtl.ca

^{c)}jacky.mardjono@safrangroup.com

^{d)}jean-philippe.groby@univ-lemans.fr

ABSTRACT

This article presents a numerical optimization procedure of continuous gradient porous layer properties to achieve perfect absorption under normal incidence. This design tool is applied on a graded porous medium composed of a periodic arrangement of ordered unit cells allowing one to link the effective acoustic properties to its geometry. The best microgeometry continuous gradient providing the optimal acoustic reflection and/or transmission is designed via a nonlinear conjugate gradient algorithm. The acoustic performances of the so-designed continuous graded material are discussed with respect to the optimized homogeneous, i.e., nongraded and monotonically graded material. The numerical results show a shifting of the perfect absorption peak to lower frequencies or a widening of the perfect absorption frequency range for graded materials when compared to uniform ones. The results are validated experimentally on 3D-printed samples, therefore, confirming the relevance of such a gradient along with the efficiency of the control of the entire design process.

Published under license by AIP Publishing. <https://doi.org/10.1063/1.5119715>

I. INTRODUCTION

Homogeneous open-cell porous materials are widely used as acoustic treatments. Their behavior is well described by propagation models, and their efficiency to operate as broadband acoustic absorbers has been theoretically, numerically, and experimentally shown for a long time. Nevertheless, they suffer from a lack of efficiency in the low frequency regime because of their intrinsic loss mechanisms. Moreover, perfect absorption is usually achieved at a single frequency, and the absorption curve presents ripples in frequency. Increasing homogeneous layer thickness is a common way to overcome this issue in order to absorb lower frequency noise. However, perfect absorption depends on the visco/inertial transition frequency,¹ therefore, limiting the lowest possible perfect absorption

frequency and the thickness of efficient treatments. In addition, thick and thus heavy treatments are unrealistic for many practical applications. Double-porosity media,² metasurfaces,^{3,4} and acoustic metamaterials⁵ are nowadays considered efficient ways to increase the low frequency attenuation/absorption. Another way consists in introducing a gradient of properties through the thickness. A correct design of such a gradient can enhance the layer absorption over a given frequency range.^{6–8} The optimal gradient is commonly described as a monotonic increase of the air flow resistivity or a decrease of the porosity of the structure through the thickness, leading to an expected continuous in frequency impedance matching at the air-porous interface. Actually, such a gradient improves absorption in the mid- and high-frequency ranges but not in the low

frequency one. Moreover, a nonmonotonic gradient can lead to better performances⁹ but are still misunderstood.

Functionally graded materials are used in many other engineering fields, mainly in mechanics, and can be precisely manufactured with various techniques.¹⁰ For instance, Han *et al.* manufactured a continuously graded bone implant by selective laser melting.¹¹ Yet, conventional porous manufacturing processes allow one to produce graded materials, e.g., graded foams⁷ or felts,⁸ but the control of the gradient is relatively low and, therefore, inaccurate for precise design. Moreover, large samples are often macroscopically inhomogeneous. No continuously graded porous acoustic treatments have yet been optimized and precisely manufactured to the author's knowledge. Fortunately, recent improvements in additive manufacturing have allowed the production of efficient acoustic treatments such as helical metamaterials,^{12,13} slow-sound based metamaterials,^{6,14} and porous open-cell materials.¹⁵ This technology enables an efficient control of the microstructure design, because the pore shapes and dimensions can be simply adjusted for the target macroscopic properties. Acoustic multilayer treatments have been manufactured by means of 3D printing such as an assembly of four layers composed of 1 mm thick microlattices,¹⁶ a superposition of microperforated panels,¹⁷ or a microperforated panel backed by a conventional felt and plenum¹⁸ as well as a superposition of two microlattice layers and a flexible membrane.¹⁹ However, these acoustic treatments consist of a small fixed number of discrete layers and were not optimized.

The aim of this article is to propose a numerical optimization procedure to design continuously graded porous acoustic materials achieving broadband perfect absorption at normal incidence. The graded properties can be directly linked to the microgeometry or the manufacturing process of the treatment. As an example, the procedure is applied to a periodic 3D printable microlattice porous material, in which the microstructure is easily tuned allowing a physical understanding of the gradient shape as well as to experimentally validate the whole process. The optimized gradients are compared to optimized homogeneous and optimized monotonic gradient layers in order to highlight the importance of such an unconstrained gradient. This optimization procedure can also be applied to any stochastic treatments manufactured by the conventional process.

The gradient optimization method is widely inspired from Ref. 20, where the characterization problem of graded porous parameter profiles was tackled by means of a conjugate gradient algorithm and the prior knowledge of the sample reflection and transmission coefficients. The present work adapts the proposed methodology to reflection and/or transmission optimization. This work distinguishes from previous one by the optimization objective, the focus on tangible variables, and the additive manufacturing proof of concept. It also differs from multilayer optimizations^{6,8,21} where a finite number of layers are fixed before the optimization. The article is organized as follows: first, the optimization procedure is introduced in Sec. II. The acoustic behavior of graded porous materials is recalled, and gradient optimization methods are detailed. Then, the optimized graded profiles and resulting absorption coefficients are presented and discussed in Sec. III. After a discussion of the optimizations, an experimental validation is carried out in Sec. IV.

II. OPTIMIZATION PROCEDURE

A. Description of the problem

The problem is depicted in Fig. 1. The porous layer is assumed to be of infinite lateral extent along the Cartesian y and z directions and is L -thick in the x direction. The normal incident plane wave is invariant in the (O,y,z) plane and propagates through the positive x direction. The inhomogeneity of the layer occurs in the x direction. Thus, as the acoustic excitation is a normal plane wave, the problem only depends on the x coordinate and thus becomes unidimensional. The surrounding and saturating fluid is air and the porous layer can possibly be rigidly backed. The interfaces of the porous layer are flat and parallel and are designated, respectively, by Γ_0 and Γ_L at $x = 0$ and $x = L$. The air medium is denoted by the superscript a . The two semi-infinite air domains are subsequently denoted by a^i and a^t to differentiate the upstream and downstream sides in the transmission case.

The analysis is performed in the linear harmonic regime at the circular frequency ω with the implicit time dependence $e^{i\omega t}$. The normal incident plane wave is expressed as $p^i = e^{-ik^a x}$, such that the pressure field in a^i reads as $p^{a^i} = e^{-ik^a x} + \mathcal{R}e^{ik^a x}$, wherein k^a is the incident wavenumber and \mathcal{R} is the reflection coefficient. If the layer is not rigidly backed, the transmitted wave takes the form $p^{a^t} = p^t = \mathcal{T}e^{-ik^a x}$, where \mathcal{T} is the transmission coefficient.

B. Geometry driven equivalent fluid model

The porous medium is modeled as an equivalent fluid medium.¹ Its acoustic properties are governed by its microstructure conditioned by the manufacturing possibilities.

1. Rigid frame and equivalent fluid approximations

The acoustic energy penetrating the porous medium is mainly dissipated through the interaction between the frame and the air saturating the pores, resulting in viscous and thermal losses. If the skeleton is sufficiently rigid, it can be assumed motionless.

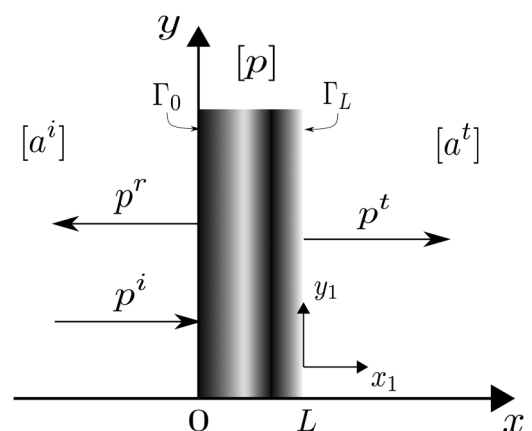


FIG. 1. x -graded porous slab. p^i is the incident wave, p^r is the reflected wave, and p^t is the transmitted wave. The incident wave is aligned with x .

The porous medium can thus be considered an equivalent fluid.¹ The considered equivalent fluid is isotropic, but the theory can simply be extended to anisotropic ones. The viscous and thermal losses in the pores are, respectively, accounted for in the equivalent density $\rho(x, \omega)$ and in the equivalent bulk modulus $K(x, \omega)$. These quantities are complex, frequency dependent, and x dependent in this study. They can be approximated by analytic, empirical, or semiphenomenological models.¹ The semiphenomenological Johnson-Champoux-Allard-Lafarge (JCAL) model^{22–24} is considered here and accounts for complicated pore morphologies by means of six parameters. According to this model, the equivalent density can be written as

$$\rho(x, \omega) = \frac{\rho^a}{\phi(x)} \alpha(x, \omega), \quad (1)$$

where ρ^a is the density of the saturating fluid, i.e., the air medium in the present case, $\phi(x)$ is the open porosity profile, and $\alpha(x, \omega)$ is the dynamic tortuosity profile. The equivalent bulk modulus can be written as

$$K(x, \omega) = \frac{\gamma P_0}{\phi(x)} \left(\gamma - \frac{\gamma - 1}{\alpha'(x, \omega)} \right)^{-1}, \quad (2)$$

where P_0 is the static pressure, γ is the specific heat ratio, and $\alpha'(x, \omega)$ is the thermal tortuosity profile.

The Johnson *et al.* model defines the dynamic tortuosity as²²

$$\alpha(x, \omega) = \alpha_\infty(x) - \frac{i\nu \phi(x)}{\omega q_0(x)} \sqrt{1 + \frac{i\omega}{\nu} \left(\frac{2\alpha_\infty(x)q_0(x)}{\phi(x)\Lambda(x)} \right)^2}, \quad (3)$$

where $\nu = \eta/\rho^a$ is the kinematic viscosity of the saturating fluid, η is the dynamic viscosity, and $\alpha_\infty(x)$, $\Lambda(x)$, and $q_0(x)$ are the high frequency limit of the tortuosity, the viscous characteristic length, and the viscous static permeability profiles of the porous medium, respectively.

The Champoux-Allard-Lafarge model further defines the thermal tortuosity as^{23,24}

$$\alpha'(x, \omega) = 1 - \frac{i\nu' \phi(x)}{\omega q'_0(x)} \sqrt{1 + \frac{i\omega}{\nu'} \left(\frac{2q'_0(x)}{\phi(x)\Lambda'(x)} \right)^2}, \quad (4)$$

where $\nu' = \nu/Pr$, Pr is the Prandtl number, and $\Lambda'(x)$ and $q'_0(x)$ are the thermal characteristic length and the static thermal permeability profiles, respectively. Therefore, a graded porous material along the thickness is that of thickness dependent porosity $\phi(x)$, high frequency limit of the tortuosity $\alpha_\infty(x)$, viscous characteristic length $\Lambda(x)$, viscous static permeability $q_0(x)$, thermal characteristic length $\Lambda'(x)$, and static thermal permeability $q'_0(x)$.

2. Equivalent fluid description: Two-scale asymptotic method

When the microstructure of the considered rigid frame material is known, the six JCAL parameters can be directly derived²⁵

and computed by means of the Finite Element Method (FEM).²⁶ The two-scale asymptotic method can be applied to periodic or stochastic media, providing a representative elementary volume (REV) where the dimensions are largely smaller than the acoustic wavelength. The REV of heterogeneous media must contain a large number of heterogeneities to be representative of the heterogeneity. If the medium is periodic, the REV reduces to the unit cell corresponding to the periodic unitary pattern. In the case of graded media, it also requires that the characteristic size of the REV is much smaller than the geometric variation, so that the assumption of the local periodicity of both materials and fields still holds.²⁵ The method consists in the application of a two-scale asymptotic homogenization to governing fundamental equations. The JCAL parameters are then calculated by integrating the computed fields. This method is detailed in Appendix A for anisotropic media. Such a numerical description of the optimized porous medium suits well to the understanding of the graded profiles because it focuses on the microgeometry. Therefore, a graded porous material through the thickness is that of thickness dependent microgeometry.

3. Geometry driven parameters and data-basis generation

The six JCAL parameters are computed for a discrete set of variables defining the porous medium architecture.

When the medium can be numerically described, the variables defining the porous medium architecture are purely geometric (pore size, pore shape, etc.) and the material can be digitally manufactured. In other words, the JCAL parameters dependence is numerically obtained from a parametric representative elementary volume.

In contrast, when the porous material is manufactured by a technique that does not give access to a precise microstructure description, the variables defining the porous medium architecture are those of the manufacturing process (compaction rate for felts, filling factor for additive manufacturing, etc.). Then, the JCAL data basis can be generated from experimental direct^{1,27} or inverse²⁸ characterization of several homogeneous samples.

To sum up, the acoustic behavior of a porous medium is driven by its microstructure. If a precise description of the latter is within easy reach, the JCAL dependence on the microstructure is digitally computed by means of a two-scale asymptotic method and the FEM. On the contrary, if a precise description is out of reach, the JCAL dependence is computed by experimental inverse characterization.

In any case, the JCAL parameters are computed for a discrete set of microstructural or manufacturing variables defining the porous medium architecture. Each JCAL parameter dependence is then obtained by interpolating a continuous and smooth function from the discrete set of computed values, thus forming a data basis for the optimization procedure.

The variables defining the microstructure of the porous medium will be the subject of the gradient optimization.

C. Acoustic waves propagation in the graded porous material

Once the JCAL parameters are linked to the architecture variables, the acoustic behavior of the graded material can be evaluated.

For clarity of the presentation, the (x, ω) dependence of ρ and K is dropped in the following.

1. Equations of macroscopically inhomogeneous porous materials under the rigid frame approximation

Using the alternative Biot's formulation,²⁹ De Ryck *et al.* derived the equations of motion in a macroscopically inhomogeneous porous material under the rigid frame approximation.³⁰ Under normal incidence, they take the usual form in the frequency domain,

$$i\omega\rho V = -\frac{\partial p}{\partial x}, \tag{5}$$

$$\frac{-i\omega}{K}p = \frac{\partial V}{\partial x}, \tag{6}$$

where p is the fluid pressure in the material pores and V is the normal equivalent velocity component for the oscillatory fluid flow in the interconnected pores. In the general case, the medium is considered anisotropic, as shown in Appendix A, with ρ being a tensor and K being a scalar. Here, the focus is put on the properties of the system along the normal incidence direction.

2. State vector formalism

The problem being unidimensional, Eqs. (5) and (6) can be directly cast in a first order differential matrix system from

$$\frac{\partial}{\partial x} \mathbf{W} - B(x)\mathbf{W} = \mathbf{0}, \tag{7}$$

wherein \mathbf{W} is the column state vector $(p, V)^\top$ and

$$B(x) = \begin{vmatrix} 0 & -i\omega\rho(x) \\ \frac{-i\omega}{K(x)} & 0 \end{vmatrix}. \tag{8}$$

Equation (7) can be directly solved via the Peano Baker series.³¹ Nevertheless, the transfer Green functions formalism is preferred because it directly provides the analytical gradient of the cost function that will be used in the optimization procedure.

3. Wave splitting and transfer Green functions formalism

The pressure and velocity fields can be decomposed in a forward, p^+ , and a backward propagating wave, p^- . By analogy with electromagnetism, where the medium is surrounded by vacuum, a "vacuum wave splitting" formulation is employed.³⁰ The pressure field is expressed in the surrounding fluid, i.e., in the air, and reads as

$$p^\pm = \frac{1}{2}(p \pm Z^a V), \tag{9}$$

wherein Z^a is the impedance of the air. This transformation is used to solve the problem, because $(p, V)^\top = (p^{[a]}, V^{[a]})^\top$ at the interface

Γ_0 (see Fig. 1). Equation (7) becomes

$$\frac{\partial}{\partial x} \begin{pmatrix} p^+ \\ p^- \end{pmatrix} - \begin{vmatrix} A^+ & A^- \\ -A^- & -A^+ \end{vmatrix} \begin{pmatrix} p^+ \\ p^- \end{pmatrix} = \mathbf{0}, \tag{10}$$

where $A^\pm = \frac{i\omega}{2} \left(\frac{Z^a}{K} \pm \frac{\rho}{Z^a} \right)$.

The two transfer Green's functions, G^+ and G^- , are now defined as follows:

$$p^\pm(x) = G^\pm(x)p^\pm(L). \tag{11}$$

By introducing Eq. (11) into Eq. (10), the first order differential system to solve now reads as

$$\frac{\partial}{\partial x} \begin{pmatrix} G^+(x) \\ G^-(x) \end{pmatrix} = \begin{vmatrix} A^+ & A^- \\ -A^- & -A^+ \end{vmatrix} \begin{pmatrix} G^+(x) \\ G^-(x) \end{pmatrix}. \tag{12}$$

These two transmission Green's functions are related to the space dependent reflection $R(x) = p^-(x)/p^+(x)$ and transmission $T(x) = p^+(L^+)/p^+(x)$ coefficients along the layer thickness via

$$R(x) = \frac{G^-(x)}{G^+(x)}, \tag{13}$$

$$T(x) = \frac{T(L)}{G^+(x)}. \tag{14}$$

The reflection and transmission coefficients of the whole porous layer are thus $\mathcal{R} = R(0)$, and the transmission coefficient is $\mathcal{T} = T(0)$. The solution of Eq. (12) is found by integrating from $x = L$, where the boundary conditions are known, to $x = 0$ using an iterative method such as the fourth order Runge-Kutta scheme.

When the porous layer is surrounded by air, the boundary conditions at $x = L$ are $R(L) = 0$ and $T(L) = 1$, which translates in the form

$$\begin{cases} G^+(L) = 1, \\ G^-(L) = 0. \end{cases} \tag{15}$$

In the opposite, when the porous layer is rigidly backed at $x = L$, the only boundary condition is $R(L) = 1$, which translates in the form

$$\frac{G^+(L)}{G^-(L)} = 1. \tag{16}$$

D. Unconstrained gradient optimization: Nonlinear conjugate gradient algorithm

The objective of the gradient optimization is to bring the reflection and/or transmission coefficients of the porous layer as close as possible to objective values by tuning a microstructure or

manufacturing parameters. The cost function J to be minimized reads as

$$J(\mathbf{q}(x)) = \sum_{\omega} W(\omega) (|\mathcal{R}(\mathbf{q}(x), \omega) - \mathcal{R}_{obj}(\omega)|^2 + |\mathcal{T}(\mathbf{q}(x), \omega) - \mathcal{T}_{obj}(\omega)|^2), \quad (17)$$

where $\mathcal{R}_{obj}(\omega)$ and $\mathcal{T}_{obj}(\omega)$ are the objective reflection and transmission coefficients, respectively, $W(\omega)$ is a frequency weighting function used to favor targeted frequency ranges, and vector $\mathbf{q}(x)$ is the microstructure or manufacturing parameters' profiles varying along the layer thickness $x = [0; L]$ and being the subject of the optimization. The goal can be to mimic the reference behavior, e.g., inverse characterization, or to optimize the absorption of the graded porous layer, e.g., when $\mathcal{R}_{obj}(\omega)$ and $\mathcal{T}_{obj}(\omega)$ are set to zero.

In this study, the absorption coefficient $\mathcal{A} = 1 - |\mathcal{R}|^2$ of the rigidly backed layer is maximized. The maximum absorption coefficient is 1, which means that perfect absorption is achieved. The objective reflection coefficient is thus zero, while no transmission is present. The optimization algorithm is detailed for the generic case.

The nonlinear conjugate gradient method³² is a generalization of the conjugate gradient method³³ that can minimize any continuous function as long as the gradient of which can be computed. The convergence to the global minimum is not ensured if the minimized function possesses local minima. This iterative algorithm steps are reminded in Appendix B. It consists in computing a search direction that will be added multiple times to the minimized function. If there is an analytic expression of the JCAL parameters' variation with respect to the graded optimized parameter, then the search direction also has an analytic form.

E. Constraint to be monotonic gradient optimization

As detailed in the Introduction, it is of interest to compare the absorption of an optimally graded porous layer to the one of an optimally graded layer in which the porosity or permeability is decreasing through the material thickness. Thus, a constraint gradient optimization algorithm is proposed. Its aim is to minimize the cost function defined by Eq. (17) by tuning a monotonically varying manufacturing or microgeometric gradient. For more clarity, only one parameter q is optimized by this algorithm. The profile of $q(x)$ is obtained by interpolating a continuous function from a discrete set of N equally spaced points $q_n = q(x_n)$, where $x_0 = 0$ and $x_N = L$. A shape-preserving piecewise cubic interpolation (Matlab, *pchip*) is used. The interpolated function is C^1 (its first derivative exists and is continuous) and respects the shape of the data. In this way, if $q_{n+1} < q_n \forall n \in [0, N]$, then $q(x)$ is monotonically decreasing. The values of q_n are optimized by means of a Nelder-Mead algorithm minimizing the cost function J and satisfying the condition $q_{n+1} < q_n \forall n \in [0, N]$.

III. NUMERICAL RESULTS

The reflection coefficient possesses pairs of poles/zeros, the location of which in the complex frequency plane $\tilde{f} = \text{Re}(\tilde{f}) + i\text{Im}(\tilde{f})$ ^{14,34} represents the system modes and their associated leakages. In the absence of losses, the zeros and poles are

perfectly symmetric with respect to the real frequency axis. Both are shifted toward the negative imaginary frequency half-space when losses are added according to the chosen time Fourier convention. Perfect absorption, i.e., $\mathcal{A} = 1 - |\mathcal{R}|^2 = 1$, is achieved when the added losses perfectly compensate for the leakage of the structure, leading to the critical coupling condition. In this respect, $20 \log(|\mathcal{R}(\tilde{f})|)$ is also plotted in the complex frequency plane to complement the analysis of the absorption coefficient. In the following, the n th zero of the reflection coefficient corresponding to the n th maximum of the absorption coefficient is noted f_{n-1} . The so-called fundamental quarter-wavelength resonance is thus f_0 .

A. Considered periodic porous medium: Microlattice porous medium

As an example, the optimization procedure is applied to the idealized microlattice graded porous layer depicted in Fig. 2. The microlattice is composed of a superposition of perfectly cylindrical parallel rods orthogonally alternating in the plane $(O, \mathbf{y}_1, \mathbf{z}_1)$. Thus, the medium is structured and periodic. Then, the REV reduces to the unit cell consisting of the junction of two orthogonal rods as highlighted in Fig. 2. The unit cell is described by two microstructural parameters: the rod diameter D , which also fixes the unit-cell thickness, and the spacing between two adjacent rods. Other equivalent parameters are the rod diameter D and the dimensionless rod step S . The latter is the spacing between two adjacent rods normalized by the rod diameter, e.g., a step $S = 1$ implies that the rods are in contact and a step $S = 2$ implies that the two rods' centers are distant from $2D$. The pore size H is defined here as the minimum distance between two adjacent rods. It is a function of S and D and is expressed as

$$H = D(S - 1). \quad (18)$$

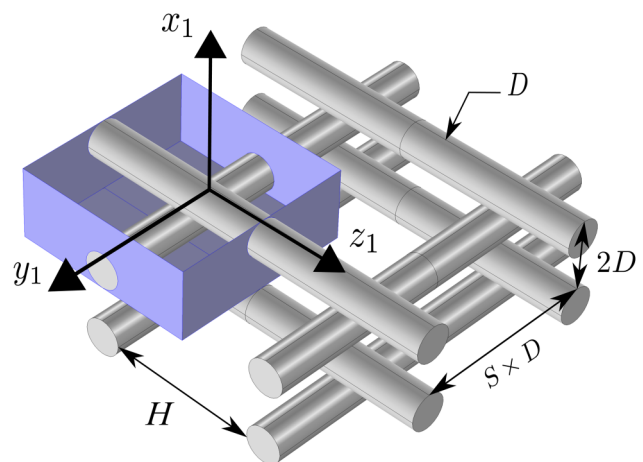


FIG. 2. Diagram of the porous material microstructure. The box delimits a unit cell. The main axis of the porous material (O, \mathbf{x}_1) is aligned with the axis of the slab (O, \mathbf{x}) . The acoustic wave propagates along $\mathbf{x} = \mathbf{x}_1$.

All the JCAL parameters of the unit cell depend on S , while the characteristic lengths and permeabilities depend also on D . For a given S , the characteristic lengths are proportional to D and the permeabilities are proportional to D^2 (see Appendix A). The porosity has a remarkably simple expression, which is given by

$$\phi = 1 - \pi/(4S). \quad (19)$$

The minimum porosity is equal to ≈ 0.21 when the rods are touching each other.

This material would be described as “quasi-isotropic” in composite science, because its in-plane properties are identical but different from the out-of-plane ones. Therefore, the microlattice material is anisotropic and its properties in the principal directions can be evaluated following the method described in Ref. 35. Nevertheless, the material principal directions fit the layer axes and rods are aligned in the plane of the layer. Only the out-of-plane properties are then considered in the present article because of the normal incidence excitation. The analysis of the anisotropic features of the present microlattice graded layer is out of the scope of the present article. The layer is thus considered isotropic in the following.

The microstructure gradients are derived from a through-the-thickness variation of S , D , or both. The rod diameter D is bounded between $D_{\min} = 100 \mu\text{m}$ and $D_{\max} = 1000 \mu\text{m}$. The dimensionless rod step S is bounded between $S_{\min} = 1.2$ and $S_{\max} = 25$. The porosity is then bounded between $\phi_{\min} = 0.35$ and $\phi_{\max} = 0.97$, while the pore size is bounded between $20 \mu\text{m}$ and 24mm .

B. Numerical settings

Both unconstrained and constraint to be monotonic gradient optimizations are numerically implemented. Continuous functions must be discretized. The microgeometric profiles are defined by 100 points. The considered graded layers are 30 mm thick leading to a discretization step of $300 \mu\text{m}$. Concerning the conjugate gradient, the number of iterations is set to 20 and the number of iterations of the line search is set to 15. These settings are found to be a good balance between computation time and convergence. The frequencies of interest are linearly spaced. The frequency weighting function W is a passband function, and its lower boundary W_{lb} and higher boundary W_{hb} depend on the optimization case. W is equal to 1 in the interval $2\pi \times [W_{lb}, W_{hb}]$ and 0 elsewhere while $0 < W_{lb} < W_{hb}$.

C. Homogeneous material acoustic behavior

Before investigating the optimal graded microlattice acoustic behavior, one of a homogeneous microlattice is first analyzed. Rod diameter D and rod step S are constant along the thickness of homogeneous materials. Figure 3(a) shows the absorption coefficient of two optimized 30 mm-thick homogeneous microlattice porous layers with the rod diameter of $D = 100 \mu\text{m}$ and $D = 400 \mu\text{m}$, respectively. Both layers are critically coupled at their respective fundamental quarter-wavelength frequencies. Absorption peaks are wider in the case of $100 \mu\text{m}$ than in the case of $400 \mu\text{m}$ rod diameter, while f_0 is slightly higher.

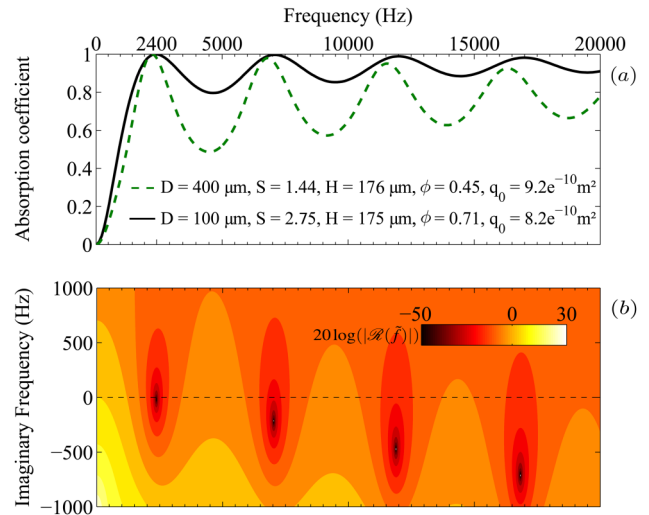


FIG. 3. (a) Hard-backed absorption coefficients of a 30 mm thick homogeneous porous layers: $100 \mu\text{m}$ rod diameter (solid line) and $400 \mu\text{m}$ rod diameter (dashed line), both structures critically coupled at f_0 . (b) Representation of $20 \log(|R(f)|)$ in the complex frequency plane of 30 mm thick porous slab, $100 \mu\text{m}$ rod diameter.

Cai *et al.*³⁶ suggested that, for an open porosity material having circular pores, the perfect absorption is obtained when the pore radius equals the viscous boundary layer thickness. The latter is linked to the visco/inertial transition frequency, for highly porous materials, as also noted by Jimenez *et al.*⁶ In our case, the porosity is usually low ($\phi < 0.9$) and the perfect absorption is achieved for a pore size H for any rod diameter, see Fig. 3(a).

Moreover, the viscous permeability decreases with the pore step S [governing ϕ and H , see Eqs. (18) and (19)] and increases with the rod diameter D [governing H , see Eq. (18)]. The lower the pore step S is and the lower the rod diameter D is, the lower the viscous permeability is. In other words, as both the pore step and the rod diameter decrease, the resistivity ($\propto 1/q_0$) increases. When perfect absorption must be attained at f_0 , a higher rod diameter is compensated by a lower rod step keeping the pore size constant but strongly lowering the porosity and slightly increasing the viscous permeability. The visco/inertial transition frequency of the material is decreased. Similarly, decreasing the rod diameter while keeping perfect absorption at f_0 shifts up the position of the poles in the absence of loss, thus decreasing the associated quality factor. Thus, the perfect absorption peaks are wider, but higher in frequency when the rod diameter is small and the rod step is optimized, as shown in Fig. 3(a). The reflection coefficient in the case of $100 \mu\text{m}$ rod diameter is plotted in the complex frequency plane Fig. 3(b). At f_0 , the zero of the reflection coefficient is exactly located on the real frequency axis, confirming the perfect absorption. For this sample, only one zero can be located on the real frequency axis at a time, i.e., perfect absorption can only be achieved at a single frequency. The losses of the following zeros are too large.

The 30 mm thick homogeneous layer, with a rod diameter of $100 \mu\text{m}$ (Fig. 3), is taken as a reference. The perfect absorption peak

frequency appears at $f_0^{ref} = 2400$ Hz. Three designs are described in Secs. III D–III F corresponding to three different goals: lowering f_0 , enhancement in the mid-frequency range of the absorption, and the broadband absorption for the same layer thickness.

D. Lowering of first perfect absorption frequency

The goal of this optimization is to lower the frequency of perfect absorption f_0 without changing the layer thickness, i.e., $L = 30$ mm by introducing a gradient of $D(x)$ and $S(x)$. Achieving perfect absorption at lower frequency for the same dimension is of particular interest because this is impossible with a homogeneous porous material and because of increasing space constraints in practical applications. Subsequently, a set of W_{lb} and W_{hb} is chosen in such a way that f_0 is as small as possible and $\mathcal{A}(f_0) > 0.995$.

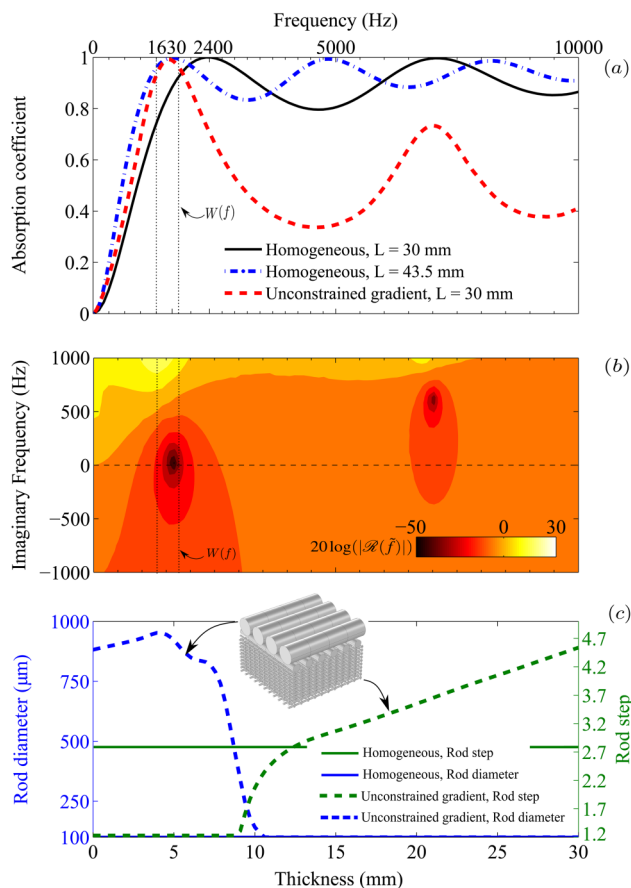


FIG. 4. (a) Hard-backed absorption coefficients of an optimized homogeneous $100 \mu\text{m}$ rod diameter 30 mm thick slab (solid line), a homogeneous $100 \mu\text{m}$ rod diameter 43.5 mm thick slab (dotted-dashed line), and a graded 30 mm thick slab (dashed line). (b) Representation of $20 \log(|R(f)|)$ in the complex frequency plane of free gradient optimized, 30 mm thick porous slab, $100 \mu\text{m}$ rod diameter. (c) Homogeneous (solid lines) and free gradient optimized (dashed lines) profiles of rod diameter (blue) and rod step (green) reducing f_0 . $W(\omega) = 2\pi[1300; 1700]$ Hz.

On the one hand, the monotonically decreasing gradient of S (and thus of ϕ and H) or D (and thus of H) does not allow to reduce f_0 with respect to f_0^{ref} . On the other hand, the lowest f_0 presenting perfect absorption that we could obtain by means of $W(\omega) = 2\pi[1300, 1700]$ Hz with an unconstrained graded layer is 1630 Hz. Figure 4(a) depicts the absorption coefficient of the reference 30 mm-thick homogeneous microlattice porous layer, the optimized unconstrained graded porous layer of the identical thickness, and an optimized 43.5 mm-thick homogeneous layer possessing perfect absorption at $f_0 = 1630$ Hz. The unconstrained optimized profiles of $D(x)$ and $S(x)$ are provided in Fig. 4(c). The thickness of the graded layer equals $\lambda/7.1$ at f_0 , where λ is the corresponding wavelength in air. The other frequency weighting functions can lead to very similar results. The absorption peak appears at a much lower frequency, but the peak is thinner and the average absorption at high frequency is degraded. Nevertheless, this result should be mitigated at first glance by the fact that the optimization algorithm has no control outside $[W_{lb}, W_{hb}]$. This is testified by the complex frequency analysis of the corresponding reflection coefficient plotted in Fig. 4(b).

The optimized profiles depicted in Fig. 4(c) present a very low rod step zone manifested at the air-layer interface and a high rod step close to the rigid backing. The high rod diameter at the air-layer interface tempers the effect of a very low rod step on the pore size, see Eqs. (18) and (19) and thus allows a low porosity while preventing the viscous permeability from falling. A continuous transition between both profiles is noticed. In other words, the optimal profile consists in a very low porosity and a medium pore size layer with a plenum, enabling to control the resonance frequency of the layer. Inside the low porosity zone, $S(x) = S_{\min} = 1.2$, i.e., $\phi(x) = \phi_{\min} = 0.34$ and $H(x) \approx 180 \mu\text{m}$, while inside the permeable zone, $D(x) = D_{\min} = 100 \mu\text{m}$, $\phi(x) \in [0.72; 0.82]$, and $H(x) \in [180; 350] \mu\text{m}$. The optimization bounds are thus reached and it would be expected to reach lower f_0 by enlarging the variation ranges, therefore, increasing the porosity drop between the two zones.

E. Medium frequencies optimization

This optimization aims at increasing the absorption coefficient between the first (f_0) and second (f_1) absorption maxima while keeping f_0 as low as possible. These two objectives being contradictory $W(\omega) = 2\pi[2000, 3200]$ Hz lead to good balance.

The monotonically decreasing gradient of S , with a rod diameter being set to $100 \mu\text{m}$, improves the absorption over the frequency range of interest by shifting f_0 up to 2600 Hz and downshifting f_1 , while widening the absorption peaks, as shown in Fig. 5(a). Perfect absorption is achieved at f_0 . The optimized rod step profile is presented in Fig. 5(c). The rod step decreases monotonically, but with a small variation. For an easier comparison, only the rod step profile is optimized in the case of the unconstrained gradient, and the rod diameter is set to $100 \mu\text{m}$. The effect of the free gradient is more pronounced than that of the constraint gradient: f_0 is still equal to 2600 Hz, while f_1 is shifted down, as depicted in Fig. 5(a). The absorption peak widths are fairly similar to the monotonic gradient optimized ones, see Fig. 5(a). As a result, absorption between f_0 and f_1 is higher than the absorption with monotonic gradient

optimization. The corresponding optimized profile is a succession of relatively closely grouped and distant rods. The variation of the rod step is greatly inferior than the one presented in Fig. 4(c). Still, it enables the control of the frequency of the first two quarter-wavelength resonances. A combined variation of the rod diameter and the rod step further increases the absorption. The rod step profile is very similar to one presented in Fig. 5(c). The diameter profile follows an inverse trend than the rod step: rod diameter is high when the rod step is low and vice versa. This two-parameter gradient shifts f_1 to a lower frequency.

F. High frequencies' optimization

Now, the maximization of the absorption coefficient over the [3000; 20 000] Hz frequency range is analyzed. The choice of $W(\omega) = 2\pi[3000; 20\ 000]$ Hz allows one to keep a perfect

absorption at f_0 . The absorption coefficient of the monotonic rod step gradient layer is higher than 0.99 between 3600 Hz and 30 000 Hz and also almost higher than 0.997 over the whole optimized frequency range as shown in Fig. 6(a). The four absorption peaks appearing at $f_n, n = 0, \dots, 3$, are shifted up in comparison to f_n^{ref} and gathered between 3000 and 20 000 Hz. Moreover, an absorption drop to 0.993 is observed between f_0 and f_1 . The rod step bell-mouth shape profile, see Fig. 6(c), begins by the maximum authorized value S_{max} . The resulting porosity profile is almost linearly decreasing. In other words, the profile presents an impedance matching. Similar to Sec. III E, only the rod step profile is optimized in the case of the unconstrained gradient and the rod diameter is again fixed at $100\ \mu\text{m}$. The absorption coefficient is

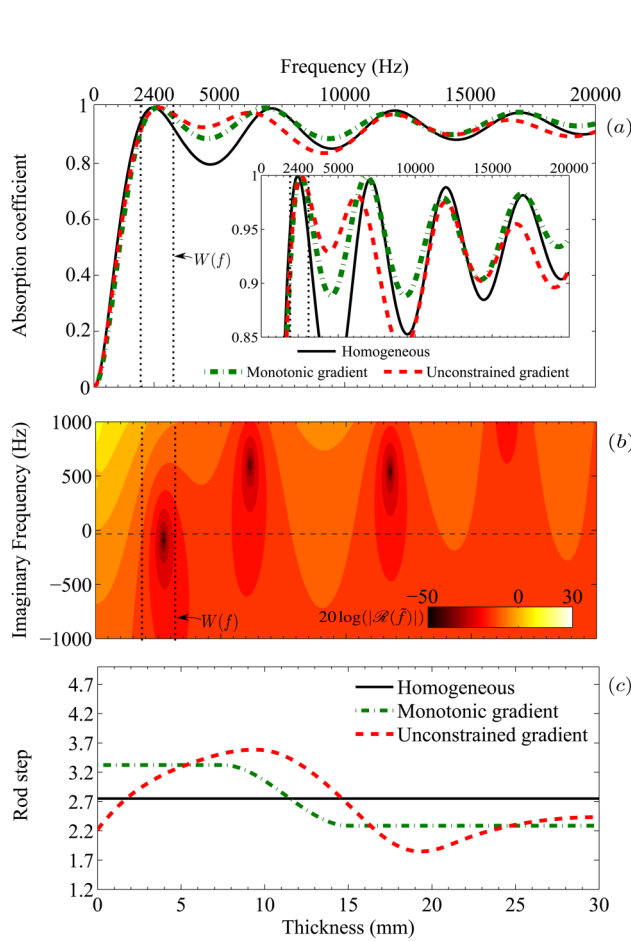


FIG. 5. (a) Hard-backed absorption coefficients of optimized 30 mm thick slabs, $100\ \mu\text{m}$ rod diameter with homogeneous rod step (solid line), monotonically graded rod step (dotted line), and free graded rod step (dashed-dotted line). (b) Representation of $20\ \log(|\mathcal{M}|)$ in the complex frequency plane of 30 mm thick, $100\ \mu\text{m}$ rod diameter, free graded rod step, porous slab. (c) Optimized graded profiles of rod step: monotonic (dashed-dotted line), and free gradient (dashed line), $D = 100\ \mu\text{m}$. $W(\omega) = 2\pi[2000; 3200]$ Hz.

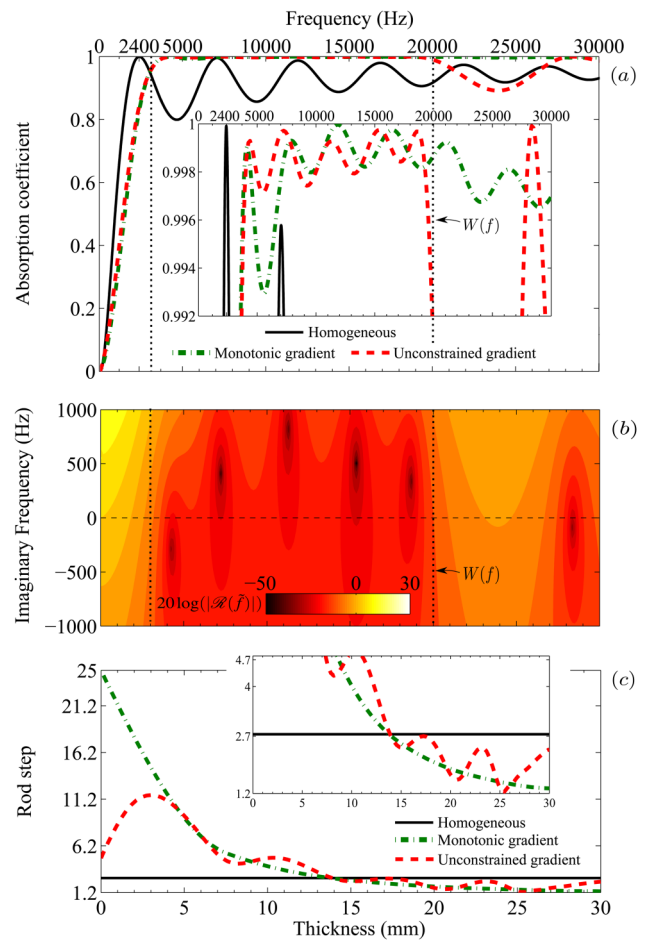


FIG. 6. (a) Hard-backed absorption coefficients of optimized 30 mm thick slabs, $100\ \mu\text{m}$ rod diameter with homogeneous rod step (solid line), monotonically graded rod step (dotted line) and free graded rod step (dashed line). (b) Representation of $20\ \log(|\mathcal{M}|)$ in the complex frequency plane of 30 mm thick, $100\ \mu\text{m}$ rod diameter, free graded rod step, porous slab. (c) Optimized graded profiles of rod step: monotonic (dashed-dotted line) and free gradient (dashed line), $D = 100\ \mu$. $W(\omega) = 2\pi[3000; 20\ 000]$ Hz.

depicted in Fig. 6(a). It is higher than 0.99 between 3600 and 20 000 Hz and higher than 0.997 between 3900 and 19 500 Hz. This improvement is possible by gathering five absorption maxima between W_{lb} and W_{hb} , as can be seen from the complex frequency analysis of the reflection coefficient depicted in Fig. 6(b). Homogeneous and graded materials with monotonically decreasing rod step only gather four absorption maxima. Furthermore, the absorption drops after W_{hb} is explained by the downwards shifting of f_5 . The rod step profile, Fig. 6(c), consists of 5 alternating relatively closely grouped and distant rods, enabling one to gather 5 modes and, therefore, 5 zeros of the reflection coefficient in the optimization frequency range. The ripples are almost removed and the absorption coefficient is almost flat over the whole frequency range of optimization.

IV. INTERPRETATION

Regardless of the optimization frequency range, an optimized unconstrained through the thickness gradient enhances the absorption properties of the material in comparison to the optimized homogeneous layer or optimized monotonic graded layer with identical thickness. Nevertheless, the previous results require comments. First, the downshifting of the first perfect absorption peak with identical thickness is necessarily accompanied by a decrease of the absorption efficiency at higher frequencies. Second, the enhancement of the absorption coefficient over a specific frequency range is always achieved at the expenses of the absorption properties outside this range. Third, broadband perfect absorption is possible if the first perfect absorption peak frequency is higher than that of the homogeneous layer. Fourth, the optimal profile is an alternating distribution of relatively closely grouped and distant rods rather than a monotonic gradient. It leads to an alternating distribution of contrasted porosity layers. This counterintuitive result is explained by the fact that the alternation enables the creation and a better control of resonances. At lower frequencies, a resonance possesses a large quality factor, thus providing a thin absorption peak. A low porosity, medium pore size layer placed in front of a plenum only possesses a single resonance at low frequency. For broadband absorption, the alternation leads to an increase of the density of states over the optimization frequency range, creating a larger number of reflection coefficient zeros located in the targeted frequency range. The absorption coefficient can, therefore, be almost flat over a wide frequency range. Nevertheless, this result might be tempered by the fact that the tuning of these modes are constrained by the thickness of the layer, thus preventing a full control of their frequency position.

V. EXPERIMENTAL VALIDATION

The optimization process is experimentally validated on samples fabricated by a Fused Deposition Modeling (FDM) Pro2 printer supplied by RAISE3D. The slicer software is Simplify3D. The cylindrical samples have a diameter and a thickness of 30 mm as depicted in Fig. 7. The extruded material is polylactic acid (PLA). The printer's nozzle is 400 μm in diameter. The targeted geometry is similar to the one described in Fig. 7. However, the orthogonal rods' layers are interlocked: the distance separating two layers oriented in the same direction is $1.5D$ instead of $2D$.

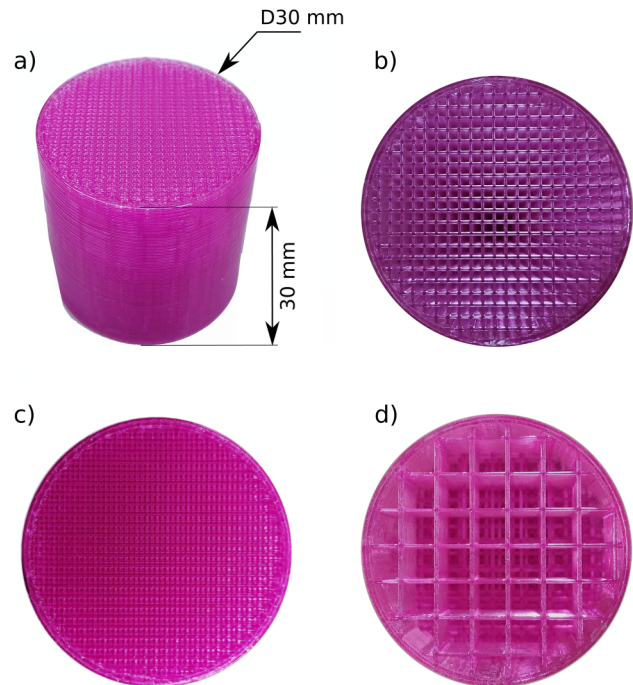


FIG. 7. (a), (b) Homogeneous samples. (c) Graded sample top view. (d) Graded sample bottom view.

Moreover, the rods are not perfectly cylindrical and their surface is scarred. Their diameter is close to the nozzle diameter. FDM and Simplify3D do not allow a direct control of the microlattice rods spacing. The manufacturing variable is the “infill factor” percentage which is inversely proportional to the spacing between two adjacent rods and can only take integer values. In this way, a graded manufacturing variable is optimized. The gradient is obtained by tuning the infill factor varying between 10% and 70%, which corresponds to a porosity of 0.90 and 0.33, respectively. A combined variation of the rod diameter and spacing would require a multinozzles printer or using another manufacturing process. Finally, an 800 μm thick solid layer surrounds the porous microlattice. Its effect is accounted for by multiplying the density and bulk modulus of the equivalent fluid by the surface of the sample divided by the surface of its porous portion.¹ The acoustic parameters are measured using a 30 mm diameter impedance tube, with a cut-off frequency of 6750 Hz. The absorption coefficient is measured using the two microphones with hard backing configuration. The measurements are performed between 500 Hz and 6000 Hz. Because of the printing inherent defects, the JCAL parameters dependence on the infill factor were obtained by the inverse characterization of a set of eight homogeneous samples followed by an interpolation over the infill factor scope.³⁷ The JCAL parameters of the characterized samples along with their interpolation (infill factor $\in [10; 70]\%$) are presented in Appendix C.

A continuous gradient, where each layer would have a different infill factor cannot be manufactured straightforwardly. Instead, a 10-layer material was printed. This number of layers is

more than sufficient to accurately discretize the continuous profile. The optimized continuous profile was thus discretized in 10 layers of identical thickness. First, the infill factor of each layer equaled the mean infill factor of the continuous profile within the layer width. Then, a Nelder-Mead algorithm adjusted the infill factor of each layer. To do so, the algorithm minimized the cost function given by Eq. (17), where $\mathcal{R}(\omega)$ is the multilayer reflection coefficient and $\mathcal{R}_{obj}(\omega)$ is the continuous profile reflection coefficient, both of them numerically computed.

Two optimizations are carried out by the unconstrained gradient algorithm. The first one considers $W(\omega) = 2\pi[1600; 1700]$ Hz in order to reduce f_0 with respect to f_0^{ref} . The second one considers $W(\omega) = 2\pi[2500; 5500]$ Hz so that the absorption is higher between f_0^{ref} and f_1^{ref} .

Figures 8(a) and 9(a) depict the absorption coefficient of the homogeneous materials, critically coupled at f_0^{ref} (TR = 55%, i.e., $\phi = 0.47$) along with the simulated and measured absorption coefficients, in both orientations, of the optimized graded materials. Figures 8(b) and 9(b) provide the corresponding continuous porosity profiles resulting from the continuously optimized infill factor profiles and their discretizations. The absorption coefficients are optimized considering the “front” orientation which corresponds to an incident wave propagating through the porosity profile from left

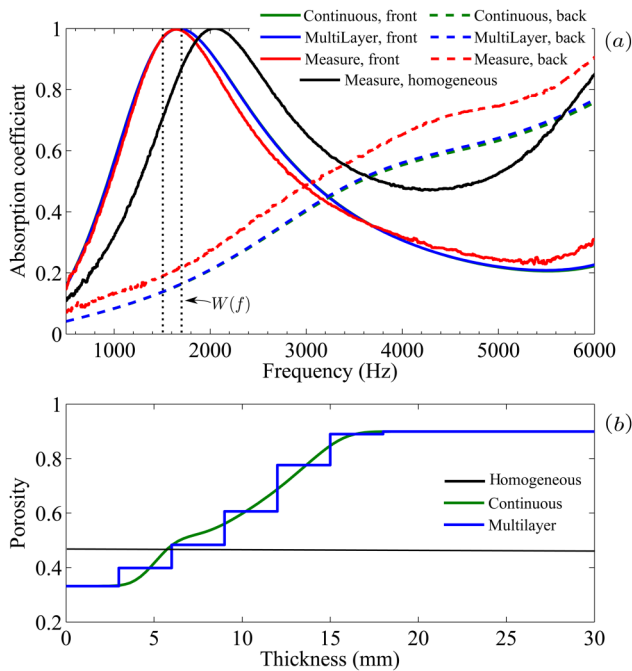


FIG. 8. (a) Rigid-backing absorption coefficients of optimized manufactured 30 mm thick slabs, numerically computed from the continuous profile (green lines), from the multilayered profile (blue lines), and measured (red lines), in direct (solid lines) and reverse (dashed lines) orientations. (b) Porosity profiles resulting from the infill factor profiles optimized by an unconstrained gradient, continuous (green line) and discretized in ten layers (blue line). $W = [1600; 1700]$ Hz.

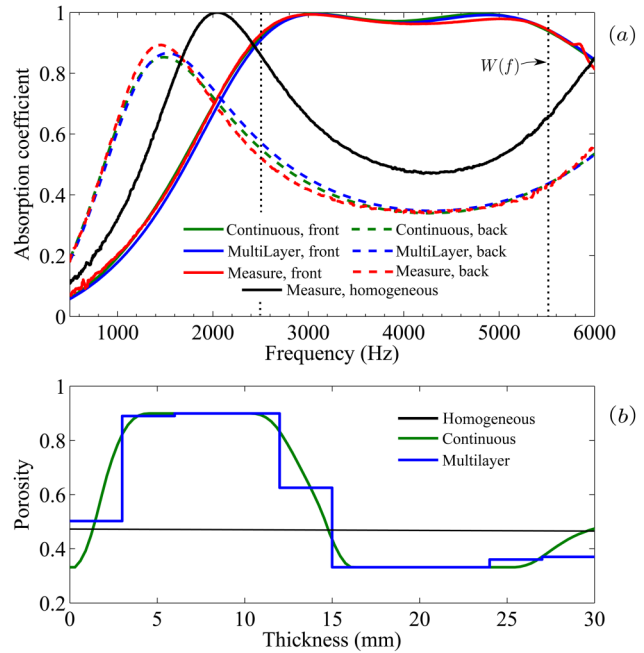


FIG. 9. (a) Rigid-backing absorption coefficients of optimized manufactured 30 mm thick slabs, numerically computed from the continuous profile (green lines), from the multilayered profile (blue lines), and measured (red lines), in direct (solid lines) and reverse (dashed lines) orientations. (b) Porosity profiles resulting from the infill factor profiles optimized by an unconstrained gradient, continuous (green line) and discretized in ten layers (blue line). $W = [2500; 5500]$ Hz.

(Thickness = 0 mm) to right (Thickness = 30 mm). The absorption coefficients are also presented considering the “back” orientation. In this configuration, the incident wave propagates from Thickness = 30 mm to Thickness = 0 mm.

For both optimizations, the continuous and multilayered profiles lead to numerically very close absorption coefficients, in both orientations, meaning that the discretization procedure is efficient.

The $W(\omega) = 2\pi[1600; 1700]$ Hz optimization resulting profile is consistent with the purely numerical one of Fig. 4(c). In both cases, the targeted frequency range is lower than f_0^{ref} and the spacing between adjacent rods ($\propto S$ and $\propto \phi$) increases along the material thickness. The measured and simulated absorption coefficients are almost superimposed in the “front” orientation, with a measured perfect absorption ($\mathcal{A} = 0.997$) at $f_0 = 1650$ Hz ($\lambda/7.1$). The correlation in the reverse (“back”) orientation is lower. The first microlattice layer of the 3D printed samples is always more resistive than expected, resulting in a difficult control of the gradient in the “back” orientation.

The medium frequencies optimization, defined by $W(\omega) = 2\pi[2500; 5500]$ Hz, creates a profile characterized by four zones alternating relatively closely grouped and distant rods, leading to low and high porosity. This profile is also consistent with the one depicted in Fig. 5(c). Moreover, there is a very good correlation between the simulated and the measured absorption coefficient, in both orientations, resulting in an absorption higher than 0.960

between 2630 and 5390 Hz, in the “front” orientation. The absorption reaches 0.994 and 0.979 at f_0 and f_1 , respectively.

VI. CONCLUSION

This work reports theoretical and experimental results for the continuous manufacturing gradient optimization of a porous layer at normal incidence. The detailed gradient optimization algorithm, adapted from an inverse characterization method, can be applied to multiple manufacturing parameters of structured periodic or stochastic media, as long as the variation of the JCAL parameters with respect to the optimized graded parameters is known.

As an example, it has been applied to rigid backing absorption optimization. The optimizations showed a significant improvement of the absorption coefficient in comparison with optimized homogeneous and monotonically graded materials. On the one hand, lowering the first perfect absorption frequency requires low porosity of the material at the air-porous interface followed by an increase. This leads to an important reduction of the absorption in the medium and high frequencies. On the other hand, increasing the absorption in the medium and high frequencies requires a porosity decrease through the thickness. It results in a shift toward high frequencies of the first maximum of absorption. The monotonic gradient widens the maxima of absorption and increases it closer to unity. The free gradient follows the same trend but adds a sequence of lower and higher porosity to the profile. The number of sequences is equal to the number of absorption maxima tuned to increase the absorption in the frequency range of interest. This results in an even higher absorption than the monotonic gradient.

Finally, experimental testing demonstrated the relevance of such gradients.

ACKNOWLEDGMENTS

The authors acknowledge Safran Aircraft Engines and the Natural Sciences and Engineering Research Council of Canada (NSERC) for supporting and funding this research. They acknowledge financial support from ANR industrial chair MACIA (No. ANR-16-CHIN-0002).

APPENDIX A: TWO-SCALE ASYMPTOTIC HOMOGENIZATION PROCEDURE

More details on two-scale asymptotic homogenization procedure can be found in Ref. 25.

1. Homogenizability conditions

A representative elementary volume (REV) is defined. It is the unit cell for periodic media (Fig. 2). Then, a characteristic dimension of the REV is selected: $l_c = D$ while the characteristic macroscopic dimension is set as $L_c = 1$ m. Separation of the scale requires that

$$\frac{l_c}{L_c} = \varepsilon \ll 1. \tag{A1}$$

For this reason, the considered microrods cannot be higher than some millimeters.

2. Double spatial variable

Two dimensionless variables are introduced. The macroscopic space variable $\mathbf{x}^* = \mathbf{X}/L_c$ and the microscopic variable $\mathbf{y}^* = \mathbf{X}/l_c$, where \mathbf{X} is the actual space variable.

The derivation operation is now written as

$$\frac{d}{d\mathbf{X}} \rightarrow \frac{d}{d\mathbf{x}^*} + \varepsilon^{-1} \frac{d}{d\mathbf{y}^*}. \tag{A2}$$

3. Asymptotic expansion

In order to separate the phenomena happening at the microscopic scale from the ones happening at the macroscopic scale, physical variables are substituted by their asymptotic expansions at multiple scales in powers of ε . A given field ψ is expressed as

$$\psi(\mathbf{x}^*, \mathbf{y}^*) = \sum_{n=0}^{\infty} \varepsilon^n \psi^{(n)}(\mathbf{x}^*, \mathbf{y}^*). \tag{A3}$$

4. Governing equations and JCAL parameters

The governing equations two-scale asymptotic formulations and the retrieved JCAL parameters are given in Appendixes A and B.

5. REV characteristic dimension

Applying a homothetic transformation to the medium microstructure and, thus, to the REV has an analytic simple effect on the medium JCAL parameters. Turning $l_c^{(1)}$ into $l_c^{(2)}$ multiplies the viscous and thermal lengths by $l_c^{(2)}/l_c^{(1)}$ and the viscous and thermal permeabilities by $(l_c^{(2)}/l_c^{(1)})^2$.

6. JCAL parameters

The homogenization procedure is applied to three fundamental equations: the mass conservation, the heat diffusion, and the momentum conservation of the saturating fluid of the REV. Ideal gas assumption, Fourier’s law, definition of the stress tensor, and Navier’s equation support the equations solving. An identification in terms of power of ε and taking the limit in $\omega \rightarrow \infty$ or $\omega \rightarrow 0$ lead to the equations of interest.

The equations are given in the generic case of anisotropic porous material for which the tortuosity, viscous characteristic length, and viscous permeability are diagonal tensors.

The thermal problem equation, taking the limit in $\omega \rightarrow 0$, reads

$$\begin{cases} \text{div}(\mathbf{grad}(\theta)) = -1, \\ \theta = 0 \quad \text{on } \Gamma_{fs}, \\ \theta \quad \Omega\text{-periodic,} \end{cases} \tag{A4}$$

where Γ_{fs} is the fluid-solid interface, Ω is the REV, and \mathbf{e}_j is the unitary vector in the REV main direction j .

In the following equations, \mathbf{k} and ξ play the role of the velocity field and its associated pressure field, respectively. The viscoinertial

problem, taking the limit in $\omega \rightarrow 0$, becomes

$$\begin{cases} \text{div}(\mathbf{grad}(\mathbf{k}_j^0)) = \mathbf{grad}(\xi_j^0) - \mathbf{e}_j, \\ \text{div}(\mathbf{k}_j^0) = 0, \\ \mathbf{k}_j^0 = 0 \quad \text{on } \Gamma_{fs}, \\ \langle \mathbf{k}_j^0 \rangle_{\Omega} = 0, \\ \mathbf{k}_j^0 \text{ and } \xi_j^0 \quad \Omega\text{-periodic}, \end{cases} \quad (\text{A5})$$

where $\langle \cdot \rangle_{\Omega}$ is the REV averaging.

The visco-inertial problem, taking the limit in $\omega \rightarrow \infty$, becomes

$$\begin{cases} \frac{i\omega\rho_0}{\eta} \mathbf{k}_j^{\infty} = \mathbf{grad}(\xi_j^{\infty}) - \mathbf{e}_j, \\ \text{div}(\xi_j^{\infty}) = 0, \\ \mathbf{k}_j^{\infty} \cdot \mathbf{n} = 0 \quad \text{on } \Gamma_{fs}, \\ \langle \xi_j^{\infty} \rangle_{\Omega} = 0, \\ \mathbf{k}_j^{\infty} \text{ and } \xi_j^{\infty} \quad \Omega\text{-periodic}, \end{cases} \quad (\text{A6})$$

The JCAL parameters are obtained by integrating, over the fluid domain Ω_f or the fluid-solid interface Γ_{fs} , the solution fields of these equations.

They are expressed as

$$\phi = \frac{\int_{\Omega_f} d\Omega_f}{\int_{\Omega} d\Omega}, \quad (\text{A7})$$

$$\alpha_{\infty} \cdot \mathbf{e}_j = \phi \langle I - \mathbf{grad}(\xi^{\infty}) \rangle^{-1} \cdot \mathbf{e}_j, \quad (\text{A8})$$

$$\Lambda \cdot \mathbf{e}_j = 2 \frac{\int_{\Omega_f} k_j^{\infty} \cdot k_j^{\infty} d\Omega_f}{\int_{\Gamma_{fs}} k_j^{\infty} \cdot k_j^{\infty} d\Gamma_{fs}}, \quad (\text{A9})$$

$$\Lambda' = 2 \frac{\int_{\Omega_f} d\Omega_f}{\int_{\Gamma_{fs}} d\Gamma_{fs}}, \quad (\text{A10})$$

$$q_0 \cdot \mathbf{e}_j = \langle k_j^0 \rangle_{\Omega}, \quad (\text{A11})$$

$$q'_0 = \frac{\int_{\Omega_f} \theta d\Omega_f}{\int_{\Omega_f} d\Omega_f}. \quad (\text{A12})$$

In the case of isotropic media, the JCAL parameters are not direction dependent: their projection over each space direction is identical. In normal incidence along \mathbf{x} , only the \mathbf{e}_x projection matters and appears in the propagation equations.

APPENDIX B: CONJUGATE GRADIENT METHOD

1. Conjugate gradient algorithm

Step 0: Initial guess

$$\mathbf{q}^{(0)}(x) = cte \forall x \in [0; L].$$

Step 1: First search direction

Set $i = 0$. Then, compute $R(x)$ and $T(x) \forall x \in [0; L]$ by means of Eqs. (13) and (14) and considering the Γ_L BC(s). Compute the gradient of the cost function

$$\mathbf{G}(\mathbf{q}^{(0)}) = \left[\frac{\partial J}{\partial q_1^{(0)}}, \frac{\partial J}{\partial q_2^{(0)}}, \dots, \frac{\partial J}{\partial q_n^{(0)}} \right]. \quad (\text{B1})$$

Set $\mathbf{D}^{(0)} = \mathbf{G}(\mathbf{q}^{(0)})$, wherein $\mathbf{D}^{(i)}$ is the search direction of iteration i .

Step 2: Line search

Compute the positive and real valued λ_i the size of which equals the one of \mathbf{q} , such that

$$J(\mathbf{q}^{(i)} - \lambda_i \mathbf{D}^{(i)}) = \min_{\lambda \in \mathbb{R}^{n+}} J(\mathbf{q}^{(i)} - \lambda \mathbf{D}^{(i)}). \quad (\text{B2})$$

The step size is obtained by an iterative method. If p depends on one parameter vector, the Golden-section search technique (Jack Kiefer, 1953) is used to find the optimal step size. Otherwise, the Nelder-Mead method is applied. This last method is a heuristic one but is fast and reliable when only a few parameters are optimized.

Step 3: Update \mathbf{q}

$$\mathbf{q}^{(i+1)}(x) = \mathbf{q}^{(i)}(x) - \lambda_i \mathbf{D}^{(i)}(x). \quad (\text{B3})$$

Step 4: New search direction

$$\mathbf{G}^{(i+1)} = \mathbf{G}(\mathbf{q}^{(i+1)}), \quad (\text{B4})$$

$$\mathbf{D}^{(i+1)} = \mathbf{G}^{(i+1)} + \beta_i \mathbf{D}^{(i)}. \quad (\text{B5})$$

β_i can be computed by the Polak-Ribiere formula with an automatic reset,

$$\beta_i = \max \left(\frac{\mathbf{G}^{(i+1)T} \mathbf{G}^{(i+1)} - \mathbf{G}^{(i+1)T} \mathbf{G}^{(i)}}{\mathbf{G}^{(i)T} \mathbf{G}^{(i)}}, 0 \right). \quad (\text{B6})$$

If i is higher than the maximum number of iterations, then the algorithm stops. Otherwise, $i = i + 1$ and loops to **Step 2**.

2. Gradient of the cost function

This section shows the details of the computation of the gradient of the cost function leading to the search direction [Eq. (B1)].

The infinitesimal variations of $R(x, \omega, \mathbf{q})$ and $T(x, \omega, \mathbf{q})$ are $\delta R(x, \omega, \mathbf{q}) = R(x, \omega, \mathbf{q} + \delta \mathbf{q}) - R(x, \omega, \mathbf{q})$ and $\delta T(x, \omega, \mathbf{q}) = T(x, \omega, \mathbf{q} + \delta \mathbf{q}) - T(x, \omega, \mathbf{q})$, respectively, resulting in a small perturbation $\delta \mathbf{q}$ of the microgeometry parameters,

$$\delta R(x = L, \omega, \mathbf{q}) = 0, \quad (\text{B7})$$

$$\delta T(x = L, \omega, \mathbf{q}) = 0, \quad (\text{B8})$$

either if the sample is rigidly backed or not because the boundary condition (surface impedance) does not depend on the material properties. From Eqs. (11), (13), and (14), the following equations are derived:

$$\frac{\partial}{\partial x} R = 2A^+R + A^-(1 + R^2), \tag{B9}$$

$$\frac{\partial}{\partial x} T = (A^+ + A^-R)T. \tag{B10}$$

Perturbing Eqs. (B9) and (B10) by $\delta\mathbf{q}$ leads to

$$\frac{\partial}{\partial x} \delta R - 2(A^+ + A^-R)\delta R = 2R\delta A^+ + (1 + R^2)\delta A^-, \tag{B11}$$

$$\frac{\partial}{\partial x} \delta T - (A^+A^-R)\delta T = T(\delta A^+ + \delta A^-R + A^-\delta R), \tag{B12}$$

wherein

$$\delta A^\pm = \frac{i\omega}{2} (Z_0\delta K_{eq}^{-1} \pm Z_0^{-1}\delta\rho_{eq}). \tag{B13}$$

The total derivative of the equivalent fluid density and bulk modulus is expressed by the addition of their partial derivatives,

$$\delta\rho_{eq} = \sum_{m=1}^n \frac{\partial\rho_{eq}}{\partial q_m} \delta q_m, \tag{B14}$$

$$\delta K_{eq}^{-1} = \sum_{m=1}^n \frac{\partial K_{eq}^{-1}}{\partial q_m} \delta q_m. \tag{B15}$$

If there is no explicit formulation of the partial derivatives, then they are computed by the derivative definition

$$\frac{\partial f}{\partial x} = \lim_{\delta x \rightarrow 0} \frac{f(x + \delta x) - f(x)}{\delta x}. \tag{B16}$$

This is the case of the partial derivative with respect to ϕ . Although it appears in the expression of ρ_{eq} and K_{eq} , the other JCAL parameters also depend in a nonanalytical way on ϕ . On the contrary, the JCAL dependence on D is fully analytic.

The variation of the cost function perturbed by $\delta\mathbf{q}$ takes the form³⁸

$$\delta J(\mathbf{q}) = 2\text{Re} \sum_{\omega} u_R(0, \omega)\delta R(0, \omega) + u_T(0, \omega)\delta T(0, \omega), \tag{B17}$$

wherein, setting $*$ as the complex conjugate notation,

$$u_R(0, \omega) = W(\omega)(\mathcal{R}(\omega) - \mathcal{R}_{obj}(\omega))^*, \tag{B18}$$

$$u_T(0, \omega) = W(\omega)(\mathcal{T}(\omega) - \mathcal{T}_{obj}(\omega))^*. \tag{B19}$$

The following integration is obtained considering the boundary condition equation (B7):

$$\int_0^L \frac{\partial}{\partial x} (u_R(x, \omega)\delta R(x, \omega) + u_T(x, \omega)\delta T(x, \omega)) = -u_R(0, \omega)\delta R(0, \omega) - u_T(0, \omega)\delta T(0, \omega). \tag{B20}$$

The right term of this equation is included in Eq. (B17). The left term's integrand can be written from Eqs. (B9) and (B10),

$$\begin{aligned} \frac{\partial}{\partial x} u_R\delta R &= \delta R \left(\frac{\partial u_R}{\partial x} + 2u_R(A^+ + A^-R) \right) \\ &\quad + u_R(2R\delta A^+ + (1 + R^2)\delta A^-), \end{aligned} \tag{B21}$$

$$\begin{aligned} \frac{\partial}{\partial x} u_T\delta T &= \delta T \left(\frac{\partial u_T}{\partial x} + u_T(A^+A^-R) \right) \\ &\quad + u_T T(\delta A^+ + \delta A^-R) + \delta R(u_T T A^-), \end{aligned} \tag{B22}$$

where $u_R(x, \omega)$ and $u_T(x, \omega)$ are arbitrary functions chosen such that the δR and δT dependencies are eliminated. In order to do this, they must satisfy

$$\frac{\partial}{\partial x} \begin{pmatrix} u_R \\ u_T \end{pmatrix} = - \begin{vmatrix} 2(A^+ + A^-R) & A^-T \\ 0 & A^+ + A^-R \end{vmatrix} \begin{pmatrix} u_R \\ u_T \end{pmatrix}. \tag{B23}$$

Equations (B21) and (B22) reduce to

$$\frac{\partial}{\partial x} u_R\delta R = u_R(2R\delta A^+ + (1 + R^2)\delta A^-), \tag{B24}$$

$$\frac{\partial}{\partial x} u_T\delta T = u_T T(\delta A^+ + \delta A^-R). \tag{B25}$$

A new expression of the variation of the cost function is then obtained by combining Eqs. (B17), (B20), (B24), and (B25),

$$\begin{aligned} \delta J(\mathbf{q}) &= -2\text{Re} \sum_{\omega} \int_0^L u_R(2R\delta A^+ + (1 + R^2)\delta A^-) \\ &\quad + u_T T(\delta A^+ + \delta A^-R). \end{aligned} \tag{B26}$$

This variation can also be simply expressed as

$$\delta J(\mathbf{q}) = \int_0^L \sum_{m=1}^n \frac{\partial J}{\partial q_m} \delta q_m. \tag{B27}$$

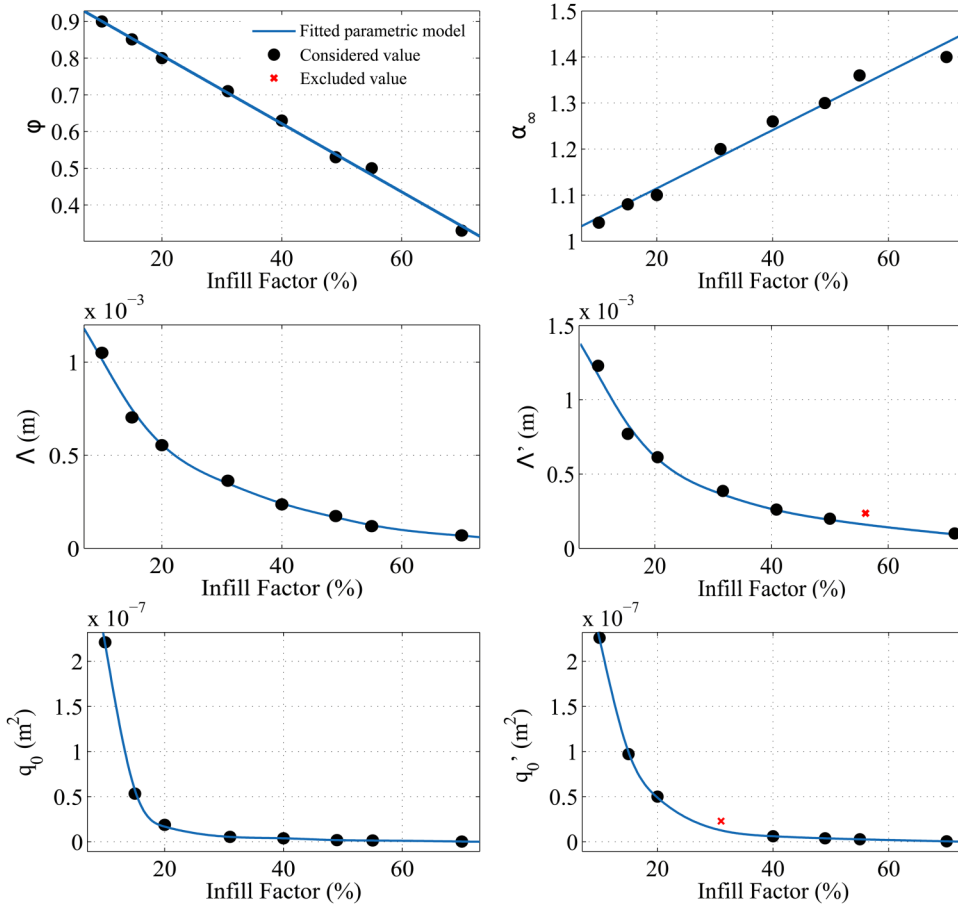


FIG. 10. JCAL parametric model, obtained by inverse characterization of homogeneous samples.

The identification of Eq. (B26) with Eq. (B27) and replacing the derivatives by their expression lead to

$$\frac{\partial J}{\partial q_i} = -\text{Re} \sum_{\omega} i\omega u_R \left(Z_0(1+R)^2 \frac{\partial K_{eq}^{-1}}{\partial q_i} - \frac{(1-R)^2}{Z_0} \frac{\partial \rho_{eq}}{\partial q_i} \right) + i\omega T u_T \left(Z_0(1+R) \frac{\partial K_{eq}^{-1}}{\partial q_i} - \frac{(1-R)}{Z_0} \frac{\partial \rho_{eq}}{\partial q_i} \right). \quad (B28)$$

APPENDIX C: JCAL EXPERIMENTAL PARAMETRIC MODEL

The “infill factor” is the manufacturing variable controlling the spacing between two adjacent rods. The JCAL parameters of eight homogeneous samples, in which the infill factor is comprised between 10% and 70 %, are retrieved by means of inverse characterization.²⁸ The manufacturing repeatability is very high which allows us to consider a single sample per tested infill factor. Finally, a numerical parametric JCAL model is obtained by interpolating over the values. It is worth noting that the interpolation functions must be continuous and monotonic. Figure 10 presents the JCAL

parameters of the homogeneous samples obtained by inverse characterization and the considered interpolated parametric functions.

REFERENCES

- J.-F. Allard and N. Atalla, *Propagation of Sound in Porous Media: Modelling Sound Absorbing Materials*, 2nd ed. (Wiley, Hoboken, NJ, 2009).
- X. Olyny and C. Boutin, “Acoustic wave propagation in double porosity media,” *J. Acoust. Soc. Am.* **114**, 73–89 (2003).
- C. Lagarrigue, J. P. Groby, V. Tournat, O. Dazel, and O. Umnova, “Absorption of sound by porous layers with embedded periodic arrays of resonant inclusions,” *J. Acoust. Soc. Am.* **134**, 4670–4680 (2013).
- J.-P. Groby, C. Lagarrigue, B. Brouard, O. Dazel, V. Tournat, and B. Nennig, “Enhancing the absorption properties of acoustic porous plates by periodically embedding Helmholtz resonators,” *J. Acoust. Soc. Am.* **137**, 273–280 (2015).
- Y. Aurégan, M. Farooqui, and J.-P. Groby, “Low frequency sound attenuation in a flow duct using a thin slow sound material,” *J. Acoust. Soc. Am.* **139**, EL149–EL153 (2016).
- N. Jiménez, V. Romero-García, and J.-P. Groby, “Perfect absorption of sound by rigidly-backed high-porous materials,” *Acta. Acust. United Acust.* **104**, 396–409 (2018).
- S. Mahasaranon, K. V. Horoshenkov, A. Khan, and H. Benkreira, “The effect of continuous pore stratification on the acoustic absorption in open cell foams,” *J. Appl. Phys.* **111**, 084901 (2012).

- ⁸J. Zhu, J. Sun, H. Tang, J. Wang, Q. Ao, T. Bao, and W. Song, "Gradient-structural optimization of metal fiber porous materials for sound absorption," *Powder. Technol.* **301**, 1235–1241 (2016).
- ⁹W. Chen, S. Liu, L. Tong, and S. Li, "Design of multi-layered porous fibrous metals for optimal sound absorption in the low frequency range," *Theor. Appl. Mech. Lett.* **6**, 42–48 (2016).
- ¹⁰M. Naebe and K. Shirvanimoghaddam, "Functionally graded materials: A review of fabrication and properties," *Appl. Mater. Today* **5**, 223–245 (2016).
- ¹¹C. Han, Y. Li, Q. Wang, S. Wen, Q. Wei, C. Yan, L. Hao, J. Liu, and Y. Shi, "Continuous functionally graded porous titanium scaffolds manufactured by selective laser melting for bone implants," *J. Mech. Behav. Biomed. Mater.* **80**, 119–127 (2018).
- ¹²X. Cai, Q. Guo, G. Hu, and J. Yang, "Ultrathin low-frequency sound absorbing panels based on coplanar spiral tubes or coplanar Helmholtz resonators," *Appl. Phys. Lett.* **105**, 121901 (2014).
- ¹³D. C. Akiwate, M. D. Date, B. Venkatesham, and S. Suryakumar, "Acoustic properties of additive manufactured narrow tube periodic structures," *Appl. Acoust.* **136**, 123–131 (2018).
- ¹⁴J.-P. Groby, R. Pommier, and Y. Aurégan, "Use of slow sound to design perfect and broadband passive sound absorbing materials," *J. Acoust. Soc. Am.* **139**, 1660–1671 (2016).
- ¹⁵E. R. Fotsing, A. Dubourg, A. Ross, and J. Mardjono, "Acoustic properties of periodic micro-structures obtained by additive manufacturing," *Appl. Acoust.* **148**, 322–331 (2019).
- ¹⁶M. D. Guild, V. M. García-Chocano, W. Kan, and J. Sánchez-Dehesa, "Acoustic metamaterial absorbers based on multilayered sonic crystals," *J. Appl. Phys.* **117**, 114902 (2015).
- ¹⁷W. Yang, S. Yuan, C. K. Chua, and K. Zhou, "Wideband sound absorption of 3d printed multi-layer micro-perforated panels," in *Proceedings of the 3rd International Conference on Progress in Additive Manufacturing (Pro-AM, 2018)*, p. 370–375.
- ¹⁸Z. Liu, J. Zhan, M. Fard, and J. L. Davy, "Acoustic properties of multilayer sound absorbers with a 3d printed micro-perforated panel," *Appl. Acoust.* **121**, 25–32 (2017).
- ¹⁹M. D. Guild, M. Rothko, C. F. Sieck, C. Rohde, and G. Orris, "3d printed sound absorbers using functionally-graded sonic crystals," *J. Acoust. Soc. Am.* **143**, 1714–1714 (2018).
- ²⁰L. DeRyck, W. Lauriks, P. Leclaire, J.-P. Groby, A. Wirgin, and C. Depollier, "Reconstruction of material properties profiles in one-dimensional macroscopically inhomogeneous rigid frame porous media in the frequency domain," *J. Acoust. Soc. Am.* **124**, 1591 (2008).
- ²¹J. S. Lee, E. I. Kim, Y. Y. Kim, J. S. Kim, and Y. J. Kang, "Optimal poroelastic layer sequencing for sound transmission loss maximization by topology optimization method," *J. Acoust. Soc. Am.* **122**, 2097–2106 (2007).
- ²²D. L. Johnson, J. Koplik, and R. Dashen, "Theory of dynamic permeability and tortuosity in fluid-saturated porous media," *J. Fluid. Mech.* **176**, 379–402 (1987).
- ²³D. Lafarge, P. Lemarinié, J. Allard, and V. Tarnow, "Dynamic compressibility of air in porous structures at audible frequencies," *J. Acoust. Soc. Am.* **102**, 1995–2006 (1997).
- ²⁴Y. Champoux and J. Allard, "Dynamic tortuosity and bulk modulus in air-saturated porous media," *J. Appl. Phys.* **70**, 1975–1979 (1991).
- ²⁵C. Auriault, J.-L. Boutin, and C. Geindreau, *Homogenization of Coupled Phenomena in Heterogeneous Media* (ISTE Ltd and Wiley, 2009) p. 476.
- ²⁶Y. Lee, M. J. Leamy, and J. H. Nadler, "Numerical calculation of effective density and compressibility tensors in periodic porous media: A multi-scale asymptotic method" in Proceedings of the COMSOL Conference, Boston, MA, 9–11 October 2008.
- ²⁷K. V. Horoshenkov, "A review of acoustical methods for porous material characterisation," *Int. J. Acoust. Vibration* **22**, 92–103 (2017).
- ²⁸M. Niskanen, J.-P. Groby, A. Duclos, O. Dazel, J. C. Le Roux, N. Poulain, T. Huttunen, and T. Lahivaara, "Deterministic and statistical characterization of rigid frame porous materials from impedance tube measurements," *J. Acoust. Soc. Am.* **142**, 2407–2418 (2017).
- ²⁹M. A. Biot, "Mechanics of deformation and acoustic propagation in porous media," *J. Appl. Phys.* **33**, 1482–1498 (1962).
- ³⁰L. De Ryck, W. Lauriks, Z. E. A. Fellah, A. Wirgin, J. P. Groby, P. Leclaire, and C. Depollier, "Acoustic wave propagation and internal fields in rigid frame macroscopically inhomogeneous porous media," *J. Appl. Phys.* **102**, 024910 (2007).
- ³¹M. Baake and U. Schlaegel, "The Peano-Baker series," *Proc. Steklov Inst. Math.* **275**(1), 155–159 (2011).
- ³²R. Fletcher, "Function minimization by conjugate gradients," *Comput. J.* **7**, 149–154 (1964).
- ³³M. R. Hestenes and E. Stiefel, "Methods of conjugate gradients for solving linear systems," *J. Res. Natl. Bur. Stand.* **49**, 28 (1952).
- ³⁴V. Romero-García, G. Theocharis, O. Richoux, and V. Pagneux, "Use of complex frequency plane to design broadband and sub-wavelength absorbers," *J. Acoust. Soc. Am.* **139**, 3395–3403 (2016).
- ³⁵A. Terroir, L. Schwan, T. Cavalieri, V. Romero-García, G. Gabard, and J.-P. Groby, "General method to retrieve all effective acoustic properties of fully-anisotropic fluid materials in three dimensional space," *J. Appl. Phys.* **125**, 025114 (2019). arXiv: 1810.03603.
- ³⁶X. Cai, J. Yang, and G. Hu, "Optimization on microlattice materials for sound absorption by an integrated transfer matrix method," *J. Acoust. Soc. Am.* **137**, EL334–EL339 (2015).
- ³⁷J. Boulvert, J. Costa-Baptista, T. Cavalieri, M. Perna, E. R. Fotsing, V. Romero-García, G. Gabard, A. Ross, J. Mardjono, and J.-P. Groby, "Acoustic modeling of micro-lattices obtained by additive manufacturing" (submitted).
- ³⁸M. Norgren and S. He, "An optimization approach to the frequency-domain inverse problem for a nonuniform LCRG transmission line," *IEEE Trans. Microw. Theory Tech.* **44**, 1503–1507 (1996).